In-situ X-ray Photoelectron Spectroscopy Study of Catalyst−Support Interactions and Growth of Carbon Nanotube Forests

Cecilia Mattevi,[‡,#] Christoph Tobias Wirth,[†,#] Stephan Hofmann,[*,†] Raoul Blume,[⊥] Mirco Cantoro,[▽] Caterina Ducati,[¶] Cinzia Cepek,[‡] Axel Knop-Gericke,[⊥] Stuart Milne,[†] Carla Castellarin-Cudia,[+] Sheema Dolafi,[+] Andrea Goldoni,[+] Robert Schloegl,[⊥] and John Robertson[†]

Department of Engineering, University of Cambridge, Cambridge CB3 0FA, U.K., Laboratorio Nazionale TASC-CNR-INFM, I-34012 Trieste, Italy, Fritz Haber Institute, D-14195 Berlin-Dahlem, Germany, IMEC, Kapeldreef 75, B-3001 Leuven, Belgium, Department of Materials Science and Metallurgy, University of Cambridge, Cambridge CB2 3QZ, U.K., and Sincrotrone Trieste SCpA, I-34012 Trieste, Italy

Received: March 20, 2008; Revised Manuscript Received: May 29, 2008

We study catalyst support interactions during chemical vapor deposition of carbon nanotubes by in situ X-ray photoelectron spectroscopy over a wide range of pressures. We observe Fe 2+ and 3+ interface states for metallic Fe on Al_2O_3 in the absence of measurable Al reduction. This support interaction is much stronger than that on SiO_2, and it restricts Fe surface mobility. The resulting much narrower Fe catalyst particle size distribution on Al_2O_3 leads to a higher carbon nanotube nucleation density and a vertical nanotube alignment due to proximity effects. We record the growth kinetics of carbon nanotube forests by optical imaging to understand effects that contribute to growth termination.

1. Introduction

Catalytic chemical vapor deposition (CVD) is the most promising growth technique for the technological integration of carbon nanotubes (CNTs) because of the ability to control location, direction, and diameter. Optimized CVD recipes can lead to the growth of dense, vertically aligned, mm-long mats or forests of multi- and single-walled carbon nanotubes (SWNTs).[1–11] The CNT alignment is caused by their high packing density, which forces vertical growth. The density of nanotubes in these CVD forests can be up to 10^{12} cm^{-2},[12,13] which is important for applications such as interconnects, heat sinks, and supercapacitors. In addition, the yield, defined as the mass ratio of nanotubes to catalyst, can be 10^5, which means that the mats are very pure. It is therefore important to understand the factors which lead to the growth of high-packing-density mats rather than isolated nanotubes or "nanotube spaghetti".

The common factor in most but not all cases of CNT forest growth is the use of Fe as a catalyst on an Al_2O_3 support layer. The role of the catalyst in CNT growth is not completely understood, but it is known that nanoparticles act as dynamic templates dictating the nanotube size distribution.[14] For thin-film-based catalysts, CNT CVD can be seen as a two-stage process: (1) the restructuring of a solid thin film into catalytically active islands and (2) graphitic network formation and actual CNT growth upon introduction of the carbon feedstock. Here, we use in situ X-ray photoelectron spectroscopy (XPS) to present a systematic study of catalyst−support and catalyst−carbon interactions during the two CVD stages for SiO_2- and Al_2O_3-supported Fe films. We focus in particular on how interface states influence catalyst mobility and therefore the catalyst size distribution during annealing at stage (1) and how this triggers CNT forest growth during C_2H_2 exposure at stage (2).

Normally, XPS is performed in UHV, whereas CNT CVD is carried out at approximately 10 orders of magnitude higher pressures. Here, we try to bridge this "pressure gap" by in situ XPS up to the mbar range, relating directly to our previous CVD experiments[15] and, more generally, to standard CVD conditions. Independent of pressure, we always observe growth-enhancing effects from Al_2O_3-supported Fe, hence indicating an apparent generality of our findings.

2. Experimental Section

We use polished Si(100) wafers as substrates, covered with 200 nm of thermally grown SiO_2. The 10 nm thick Al_2O_3 support layers are magnetron sputtered. We refer to $Al_2O_3/SiO_2/Si(100)$ as the Al_2O_3 support. Fe catalyst films are both ex situ deposited with subsequent transfer in air and in situ deposited in UHV (base pressure $< 10^{-10}$ mbar) without breaking the vacuum prior to XPS analysis. The in situ deposited catalyst films are e-beam evaporated at a rate of ∼0.1 nm/h. The deposition rate is obtained from the attenuation of the photoemission peaks of Al 2p for the Al_2O_3 and Si 2p for the SiO_2 support layer. The ex situ deposition of Fe is carried out in a thermal evaporator. The evaporation rate is kept at about 1 Å/s at $<10^{-6}$ mbar of base pressure. The nominal, mean film thickness is monitored in situ by a quartz crystal microbalance and calibrated ex situ by atomic force microscopy (AFM, Veeco Explorer) and spectroscopic ellipsometry (Woollam, M-2000 V).

UHV-XPS Fe 2p spectra are acquired in normal emission geometry using a conventional Mg X-ray source ($h\nu = 1253.6$

* To whom correspondence should be addressed. E-mail: sh315@cam.ac.uk.
# These authors contributed equally.
‡ Laboratorio Nazionale TASC-CNR-INFM.
† Department of Engineering, University of Cambridge.
⊥ Fritz Haber Institute.
▽ IMEC.
¶ Department of Materials Science and Metallurgy, University of Cambridge.
+ Sincrotrone Trieste SCpA.

10.1021/jp802474g CCC: $40.75
Published on Web 07/22/2008

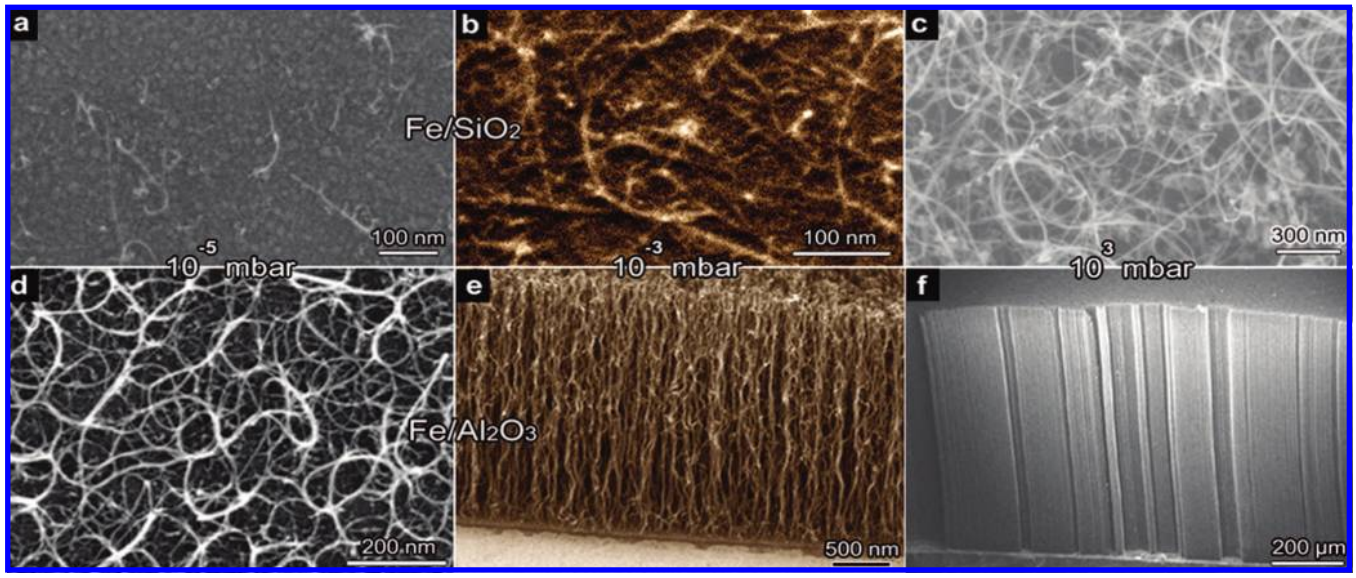

Figure 1. SEM images of CNTs catalyzed by SiO_2-supported (a−c) and Al_2O_3-supported (d−f) Fe films in C_2H_2. (a,d) CVD at 8×10^{-5} mbar of C_2H_2 for 5 min at 580 °C from an in situ deposited Fe film (0.5 nm). The catalyst film was annealed prior to growth in UHV for 5 min. (b,e) CVD at 2.5×10^{-3} mbar of C_2H_2 for 5 min at 500−580 °C from an ex situ deposited Fe film (0.5 nm) annealed in NH_3 for 5 min. (c,f) Atmospheric pressure CVD performed in a conventional 2 in. tube furnace (Carbolite) with a custom-built direct heater loaded into the quartz tubing (cold-wall conditions). CNTs are grown at ∼750 °C in 200:500:10 sccm of $Ar/H_2/C_2H_2$ for 17 min from an ex situ deposited Fe film (0.9 nm).

eV) with an overall energy resolution of ∼1.1 eV. The high-pressure XPS experiments are performed at the BESSY synchrotron in the end station of the FHI-MPG. The high-pressure setup consists mainly of a reaction cell attached to a set of differentially pumped electrostatic lenses and a differential-pumped analyzer, as described elsewhere.[16] There, all spectra are collected in normal emission at photon energies of 435 eV (C 1s) and 800 eV (Fe 2p3/2), respectively, with a spectral resolution of ∼0.3 eV. For these photon energies, the electron mean free path, λ, varies between 4 to 7.5 Å, and the XPS information depth is ∼2 nm, that is, 95% of all detected electrons originate from 3λ.[17] For XPS analysis, the photoelectron binding energy (BE) is referenced to the Fermi edge, and the spectra are normalized to the incident photon flux. Background correction is performed by using a Shirley background.[18] The spectra are fitted following the Levenberg−Marquardt algorithm to minimize χ^2. Peak shapes are modeled by asymmetric Doniach−Sunjic functions convolved with Gaussian profiles.[19] The accuracy of the peak positions for different fits is ∼0.05 eV.

To address the "pressure gap", CNT CVD is performed in high vacuum, in the mbar range, and at atmospheric pressure. The carbon nanostructures are analyzed by scanning electron microscopy (SEM, Jeol 6340 and LEO 1530VP FEGSEM), high-resolution transmission electron microscopy (HRTEM, Jeol JEM 4000EX, 400 kV), and Raman spectroscopy (Renishaw 1000 Raman spectrometer, at 514.5, 633, and 785 nm excitation).

3. Results

3.1. Effect of Oxide Support on CNT Growth Behavior. Figure 1 summarizes our CNT growth results.[15,20,21] The SEM images compare CNTs nucleated from SiO_2-supported (Figure 1a−c) and Al_2O_3-supported (Figure 1d−f) subnanometer Fe films (0.5−0.7 nm) after C_2H_2 exposure at three different partial growth pressures in three different deposition systems. We see that, at each growth pressure, the oxide support layer has a significant influence on the CNT yield and morphology. In general, the CNT yield for the SiO_2-supported Fe catalyst is much lower than that for Al_2O_3-supported Fe. Figure 1a,d shows CNTs grown at 8×10^{-5} mbar and 580 °C from an in situ deposited, UHV-annealed 0.5 nm thick Fe catalyst film. At these low pressures, isolated SWNTs form on the SiO_2 surface (Figure 1a), while a dense lateral mat of SWNT bundles forms on the Al_2O_3 support (Figure 1d). Figure 1b,e shows CNTs grown at 2.5×10^{-3} mbar and ∼500−580 °C from a 0.5 nm thick NH_3-annealed Fe film. Whereas the SWNTs form a network of long, bundles on SiO_2 (Figure 1b), they form a vertically aligned, 3 μm high forest on the Al_2O_3 support (Figure 1e). Figure 1c,f shows CNTs grown at atmospheric pressure and 750 °C. The ∼0.7 nm thick Fe film was annealed in Ar and H_2. MWNT forests, up to a few mm thick and a density of $\sim 10^{10}$ CNTs/cm^2, nucleate on the Al_2O_3 support (Figure 1f), whereas on SiO_2, the MWNT density is too low for vertical alignment (Figure 1c).

3.2. XPS Analysis of Catalyst−Support Interactions. We first study the interaction of the Fe catalyst with the oxide support layers and its restructuring at stage (1). Figure 2a,b compares the Fe 2p3/2 core level spectra for as-deposited Fe thicknesses ranging from <0.1 to ∼0.6 nm. For SiO_2, we observe only a metallic Fe component at 707.3 eV (Figure 2a). In contrast, on Al_2O_3, the Fe 2p3/2 spectra also show Fe^{2+} and Fe^{3+} oxide states at 710.3 and 711.9 eV, respectively (Figure 2b). The Al 2p band is not shifted during Fe evaporation (not shown); hence, we can exclude Al reduction or formation of metallic Fe−Al species. These results are consistent with previous studies of the Fe/Al_2O_3 interface by XPS[22] and Auger electron spectroscopy (AES).[23]

The formation of these Fe oxide states indicates a strong interaction between Fe and the surface oxygen atoms of the alumina support. We note that the relative intensity between the metallic and oxidized peaks increases as a function of Fe coverage. The Fe 2+/3+ signals disappear above an Fe thickness of ∼0.6 nm (Figure 2b). Johnson et al.[24] explained this interaction by the formation of Fe−O bonds at the metal−Al_2O_3 interface, whereas Diebold et al.[25] pointed out possible charge transfer from the Fe to the surface oxygen atoms.

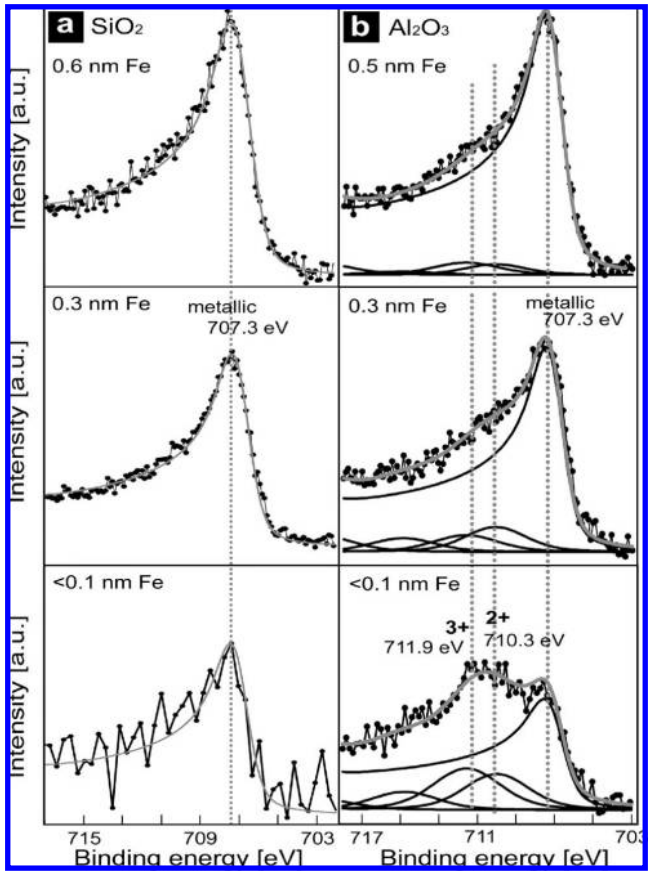

Figure 2. Fe 2p3/2 XPS spectra ($h\nu = 1253.6$ eV) of (a) Fe deposited on a SiO_2/Si substrate in UHV at ~RT for thicknesses of <0.1, 0.3, and 0.6 nm and (b) of Fe deposited on an Al_2O_3/SiO_2/Si substrate in UHV at ~RT for thicknesses of <0.1, 0.3, and 0.5 nm. The metallic Fe^0 component is centered at 707.3 eV, the Fe^{2+} peak at 710.3 eV, and the Fe^{3+} component at 711.9 eV. The spectra on the bottom, middle, and top are multiplied, respectively, by a factor 5, 2, and 1.2 with respect to normalization to incident photon flux.

Figure 3a,b compares Fe 2p core level spectra obtained for ~0.3 nm thick Fe on SiO_2 and Al_2O_3 at room temperature and after annealing at 580 °C in UHV. Upon annealing of SiO_2-supported Fe, the Fe 2p peak height decreases by about 35%. No contributions of Fe^{2+} and Fe^{3+} states are detected. This characterizes the weak interface interactions between Fe and SiO_2. In contrast, for Fe on Al_2O_3, the total area under the Fe 2p line remains nearly constant upon annealing, while the Fe 2p line shape changes slightly (Figure 3b). The Fe^{2+} component disappears due to a transition to more stable Fe^{3+} oxidation.[26,27] Furthermore, a marginal decline of the metallic peak can be observed which relates to a slight coarsening of the Fe film. The Al_2O_3 support tends to stabilize interfacial Fe oxidation states, and we argue that this is what prevents excessive coalescence of Fe particles. On the other hand, on SiO_2, Fe coalesces into larger islands. We can confirm this behavior also for ex situ deposited Fe.

3.3. Ex Situ AFM and TEM Characterization of Catalyst−Support Interaction. AFM and TEM analyses are carried out to determine the morphology and size distribution of catalyst particles. The samples are processed in the same CVD conditions that yielded growth of mm-thick forests. The measurements are performed at ambient conditions, and therefore, oxidation effects must be taken into account.[28,29] Figure 4 shows an AFM characterization of 1.1 nm Fe films, as-evaporated at room temperature and after annealing at 750 °C in an Ar/H_2 atmosphere on SiO_2 and Al_2O_3 supports. Prior to annealing, the

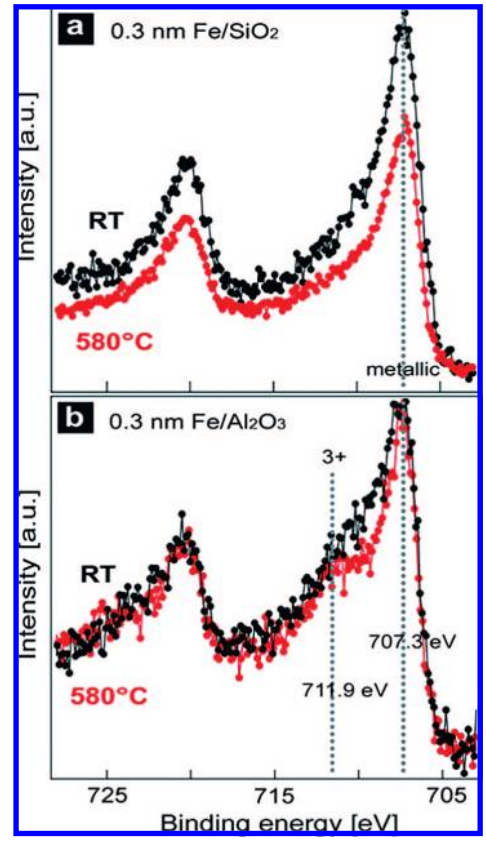

Figure 3. Fe 2p XPS spectra ($h\nu = 1253.6$ eV) of ~0.3 nm thick Fe evaporated and annealed on (a) SiO_2/Si and (b) Al_2O_3/SiO2/Si. Fe is in situ deposited in UHV (5×10^{-9} mbar background pressure) at ~RT. The annealing step was performed at ~580 °C at 2×10^{-10} mbar for 5 min. All spectra are normalized to the photon flux.

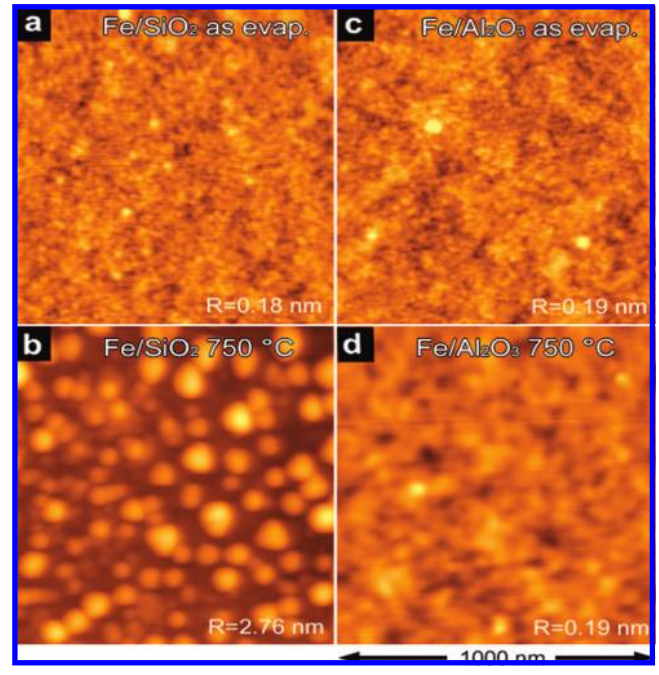

Figure 4. AFM topography images of as-evaporated and subsequently annealed Fe (~1.1 nm) films on (a,b) SiO_2/Si and (c,d) Al_2O_3/SiO2/Si. The catalyst films are annealed at 750 °C at atmospheric pressure in 200:500 sccm of Ar/H_2 for 3 min.

Fe films are relatively smooth and have a similar roughness of 0.18−0.19 nm root-mean-square (rms) on SiO_2 and Al_2O_3 (Figure 4a,c). Figure 4b shows that the rms roughness increases

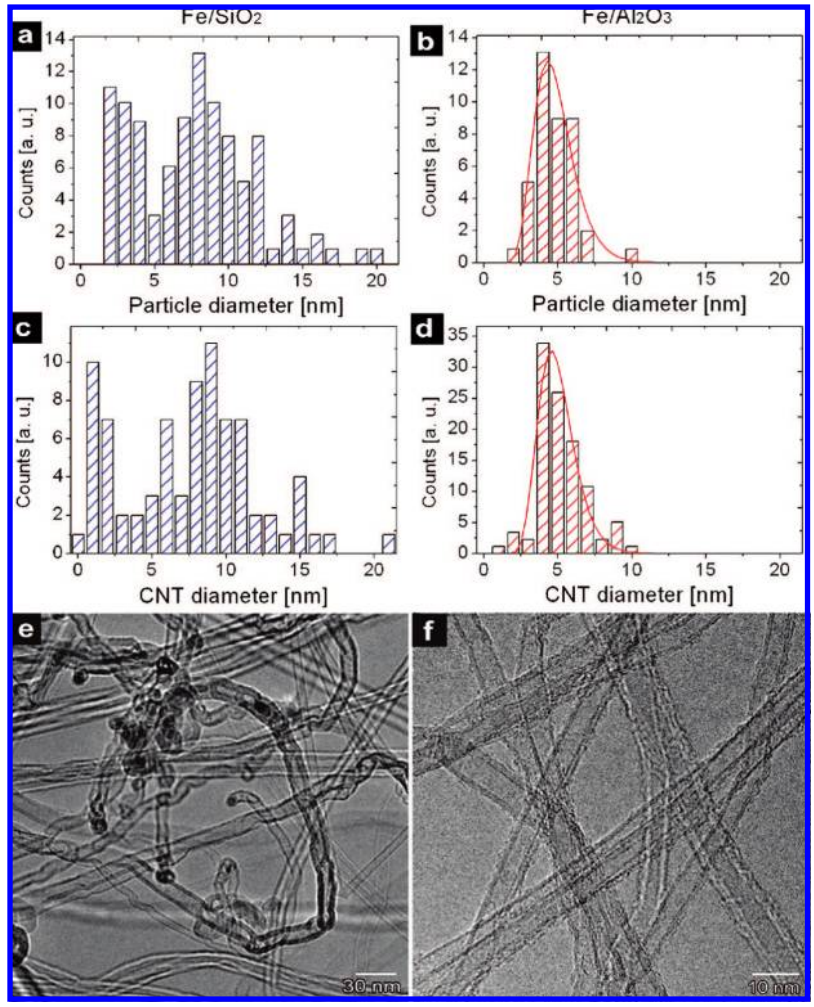

Figure 5. Catalyst particle size and CNT diameter distributions extracted from high-resolution TEM images of ~0.7 nm Fe supported on (a,c,e) SiO_2 and (b,d,f) Al_2O_3 electron-beam-transparent membranes exposed to 750 °C for 2 min at atmospheric pressure in 200:500 sccm of an Ar/H_2 flow in a 2 in. tube furnace.

about 15-fold upon annealing of Fe on SiO_2, while for Al_2O_3-supported Fe, the roughness remains roughly constant (Figure 4d). Fe de-wets SiO_2 so that some areas become completely Fe-depleted (Figure 4b). The resulting Fe nanoislands coarsen by cluster migration or Ostwald ripening.[30,31] The coalescence is driven by a minimization of the surface free energies and the free energy of the support−metal interface.[31–34] In comparison, Fe coarsens significantly less on Al_2O_3 (Figure 4d). In combination with the XPS results, this confirms that the strong interaction between Fe and Al_2O_3 lowers the Fe mobility.

Figure 5 shows the particle size distributions and resulting CNT diameters extracted from high-resolution TEM images (Figure 5e,f) of CNTs catalyzed by ~0.7 nm Fe supported on SiO_2 and Al_2O_3 electron-transparent membranes. We see that the Fe particle size distribution on SiO_2 is much broader than that on Al_2O_3 (Figure 5a,b). The particle size distribution on Al_2O_3 has a single, narrow peak at ~5 nm, confirming in agreement with the XPS and AFM measurements that Al_2O_3 restricts the coalescence of Fe particles. The corresponding CNT diameter distribution (Figure 5c,d) reflects that of the catalyst islands.[35] Fe-catalyzed CNTs have diameters in the range of 2−18 nm on SiO_2 and 2−8 nm on Al_2O_3 support.

3.4. XPS Analysis of CNT CVD. Figure 1 showed that for the same CVD conditions, Fe/Al_2O_3 gives a much higher CNT yield compared to that of Fe/SiO_2. Noda et al.[8] attributed this CNT growth enhancement to the catalytic activity of Al_2O_3 for hydrocarbon dissociation. To test this idea, we monitored the C 1s core level line while annealing and exposing bare Al_2O_3 substrates to C_2H_2 (Figure 6a). Initial C contamination related to air transfer was removed by preannealing in O_2. Figure 6a clearly shows that for our conditions, no carbon is deposited on the Al_2O_3, that is, no C 1s is detected. XPS measurements performed in the UHV system gave similar results. We thus rule out any significant contribution to CNT growth by catalytic C_2H_2 dissociation on the Al_2O_3 substrate itself.

In contrast, for Fe-covered Al_2O_3, we observe the rise of a "graphitic" peak at 284.55 eV due to sp^2-hybridized C−C bonds of CNTs formed during C_2H_2 exposure (Figure 6b). We measured the Fe−C_2H_2 interaction during CNT growth in situ, time-resolved at ~2.5×10^{-3} mbar of C_2H_2. A weak C contamination peak is observed initially at ~286 eV. The intensity of the graphitic peak increases very rapidly and saturates after ~114 s. The C 1s XPS signal saturates well before CNT growth termination, primarily due to screening by the CNTs. The evolution of the C 1s peak is basically the same as that measured on SiO_2, except that the measured signal intensity is about 8 times higher on Al_2O_3 than that on SiO_2. This difference is due to the greater nanotube density within the probe depth for the forests formed on Al_2O_3 (Figure 1).

Arcos et al.[36] concluded that oxidized Fe particles are an efficient catalyst for C_2H_2 decomposition. We therefore oxidized 0.25 nm of Fe on Al_2O_3 by exposing to O_2 at ~600 °C prior to

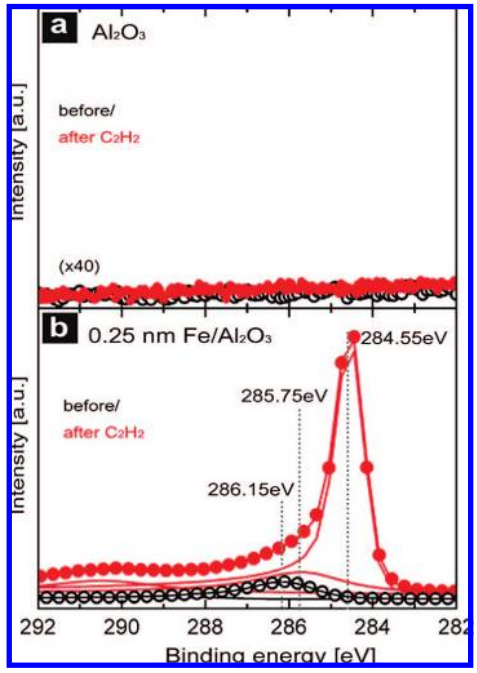

Figure 6. (a) C 1s XPS spectra of a bare $Al_2O_3/SiO_2/Si$ substrate before and after exposure to ~2.5 × 10^{-3} mbar of C_2H_2 at ~600 °C. The sample was pretreated in O_2 (~10^{-2} mbar) and NH_3 (~0.6 mbar). (b) C 1s XPS spectra of ~0.25 nm of Fe on an $Al_2O_3/SiO_2/Si$ substrate before and after C_2H_2 exposure as in (a). The sample was pretreated in NH_3 (~1 mbar). All spectra are normalized to the photon flux.

C_2H_2 exposure at 2.5 × 10^{-3} mbar. We find that C_2H_2 does not significantly reduce Fe oxides under our CVD conditions, and we observe no CNT growth for oxidized Fe. This suggests that Fe is active for CNT growth in its metallic state and that Fe has to be at least partly reduced during stage (1) of the CVD process. The carbon potential during stage (2) can lead to intermittent Fe carbide formation.[14,37]

3.5. Growth Kinetics and Catalyst Deactivation. Understanding catalyst activation and growth termination is critical for CNT growth at high yield.[38] There have previously been a number of in situ and ex situ measurements of growth kinetics using various techniques such as laser interference,[2,39] absorbance,[40] diffraction,[41] and optical imaging.[41–43] The detailed mechanisms that cause growth termination are still unclear. Figure 7a shows optical imaging of CNT forest growth at atmospheric pressure conditions in our tube furnace. We set a standard digital camera to take an image every 2 s (see Supporting Information). Figure 7b plots the forest thickness versus reaction time at three different positions along the substrate. The CNTs follow a base growth mechanism.[44] Figure 7c shows SEM images of the different stages of forest nucleation. Initially, randomly orientated CNTs are forced into a vertical alignment due to a proximity effect of sufficiently densely distributed active catalyst particles.[45] Vertical CNT alignment is reached within a forest thickness of few μm, which corresponds to a growth time of only few seconds.

The forest height saturates after ~10 min. We extrapolate an average growth rate of about 500 μm/min. A three-walled CNT 5 nm in diameter has ~1600 carbon atoms per nm length; hence, the growth rate corresponds to the incorporation of ~10^7 carbon atoms per second. This is fully consistent with CNT growth extrusion from a metallic Fe catalyst particle based on Fick's law, with a diffusion coefficient (at 750 °C) of ~2 × 10^{-10} m^2/s and C solubility of ~0.03 weight% in bcc Fe.[46] Growth of packed SWNT forests with a density on the order of 10^{12} cm^{-2} can be limited by diffusion of the carbon precursor through already grown CNTs.[13] The density of our MWNT forests, however, is too low (<~10^{10} cm^{-2}) to attribute CNT growth deceleration to such a diffusion limit.[47] Figure 7b shows that the initial transient of the forest height and the abrupt growth termination cannot be fitted by a single exponential decay function.[38] The saturation behavior is convolved with the temperature profile and instabilities of the direct heating. We think that in particular for position 2, a raise in temperature caused the catalyst poisoning, possibly due to support interactions. We note that self-termination of forest growth is accompanied by loss of CNT alignment in the bottom layer.[48] This may be caused by a decreasing amount of active catalyst particles.

4. Discussion

We observe Fe 2+ and 3+ interface states for metallic Fe on Al_2O_3 in the absence of measurable Al reduction. This support interaction is much stronger than that on SiO_2 and restricts Fe surface mobility. This is consistent with the observations of Fe^{2+} states for Fe monolayers on Al_2O_3.[22] It is also consistent with the general picture of the behavior of metals on oxide supports.

Diebold et al.[49] noted that the more electronegative transition metals at the right-hand end of the transition series tend to de-wet and form islands when deposited at room temperature on TiO_2 surfaces and become encapsulated within an oxide shell when heated (Figure 8). On the other hand, the more electropositive metals tend to wet oxide layers, grow by layer-by-layer growth, and tend not to de-wet upon annealing (Figure 8). Campbell[50] related this change to the difference of adhesion energies for the two cases. Diebold et al.[49] noted that the more electronegative metals did not reduce the TiO_2 surface, whereas the more reactive, electropositive metals reduced one or more layers of the TiO_2, thereby forming an interfacial bond which increased their adhesion energy. This behavior pattern can be related to the oxide free energy of formation per O atom.[51] This increases (negatively) as the metal work function decreases,[52] that is, the more electropositive the metal (Figure 9).

A strongly electropositive metal will displace Ti from its oxide, TiO_2, because of its greater affinity for oxygen. However, less electropositive metals can still displace some O from the TiO_2 because they create surface vacancies in the TiO_2, which costs less than the bulk reaction. Fe is therefore at the boundary of this interaction. It is electronegative enough that it de-wets on TiO_2 surfaces, but it is reactive enough to just displace some O and to slightly reduce the TiO_2 surface and form O vacancies, with a strong metal−support interaction. This argument has been developed for the case of metals on TiO_2, which have been studied in more depth. TiO_2 is of course a mixed-valence metal. Nevertheless, Al and Ti have similar work functions (~ 4.3 eV, Figure 9), so that we argue that Fe on Al_2O_3 behaves similarly to Fe on TiO_2. It is electronegative enough to de-wet but reactive enough to have a strong interaction which stops it sintering at higher temperatures.

The strong specific interface between iron and alumina has been studied extensively in the context of ammonia synthesis, for which alumina is a critical promoter to iron catalysts.[53] UHV model studies showed a restructuring of iron single crystals due to strain and an interface compound formation with alumina nanostructures.[54] In analogy to the present observations, these strong interactions prevailed also under 20 bar of pressure of hydrogen and temperatures exceeding 673 K.[54]

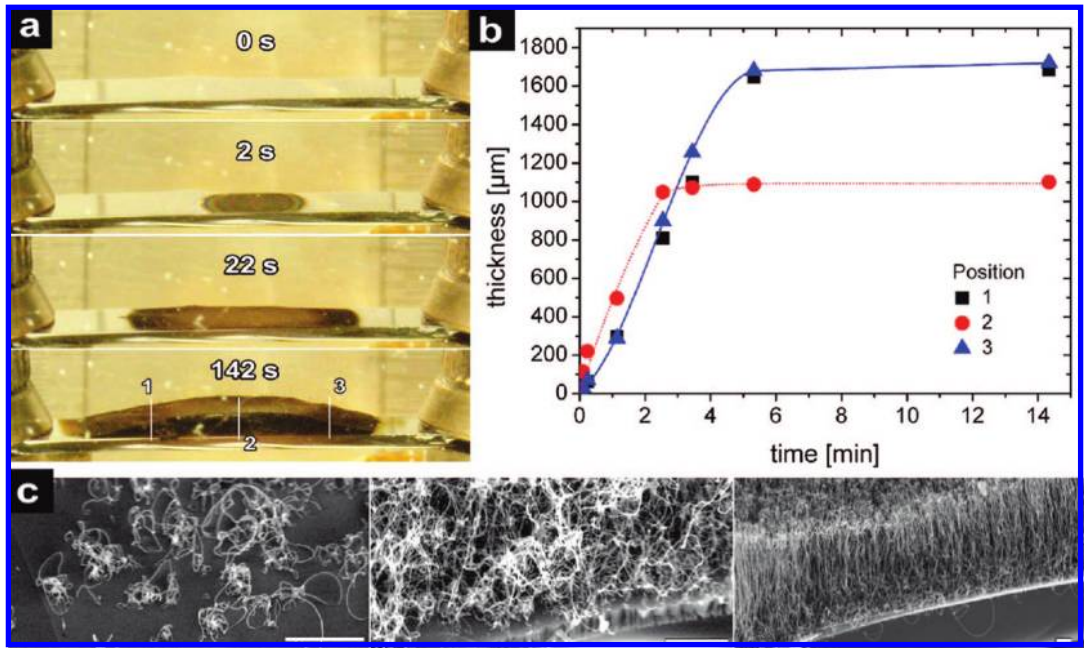

Figure 7. (a) Optical imaging of Fe(0.9 nm)/Al_2O_3-catalyzed CNT forest growth for 200:500:10 sccm of Ar/H_2/C_2H_2 in an atmospheric tube furnace (see Supporting Information). The Si substrate shows an approximately Gaussian temperature profile centered initially at ~750 °C due to direct heating. The terminal CNT forest thickness is ~1.8 mm. (b) CNT forest thickness plotted versus growth time for three different positions indicated in (a); lines serve as a guide to the eye. (c) SEM images of various positions along the CNT forest interrupted at early stages of growth at conditions similar to those in (a). Scale bars: 1 μm.

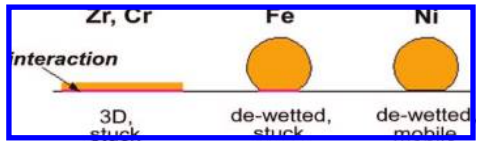

Figure 8. Schematic of the metal−oxide surface interaction. A reactive, electropositive metal, such as Zr or Cr, wets and interacts strongly with the oxide (left). Fe does not wet the oxide but still interacts quite strongly with the oxide surface (middle). Electronegative metals like Ni do not wet the surface and interact weakly with the metal (right).

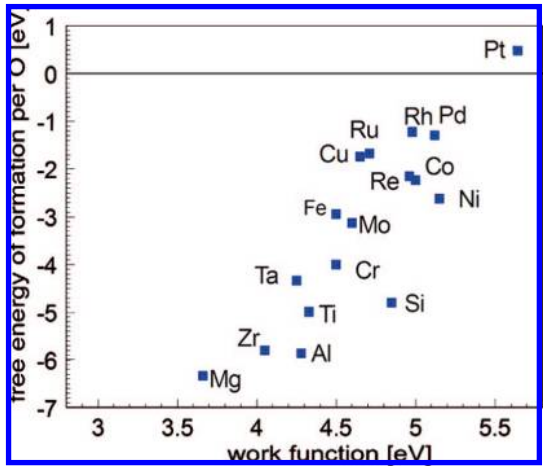

Figure 9. Free energy of MO_x formation per oxygen atom plotted versus the work function.

5. Conclusion

We conclude that the use of an Al_2O_3 support layer increases the yield of Fe-catalyzed CNT growth over a wide range of CVD conditions due to the specific character of the Fe/Al_2O_3 interface reaction. The formation of Fe 2+ and 3+ interface states on Al_2O_3 restricts Fe surface mobility, resulting in a narrow catalyst particle size distribution and the nucleation of vertically aligned CNT mats. We have shown that the high-valent states of iron are not reduced during CNT synthesis. It is speculated that the details of the interfacial bonding between iron and alumina with the possibility of iron aluminate interface compounds and the generation of substantial lattice strain in the metal particles are the origin of this kinetic stability. At the conditions used, the Al_2O_3 substrate itself showed no catalytic activity for C_2H_2 decomposition, and we showed that Fe is active for CNT growth only in its metallic state.

Acknowledgment. Support by the European Community (IP CANAPE, Contract No. 500096) is gratefully acknowledged. S.H. acknowledges funding from The Royal Society and Peterhouse, Cambridge. We wish to thank M. Albrecht, A. Oestereich, M. Haevecker, and the Bessy staff for experimental support.

Supporting Information Available: Side view image sequences (H.264 encoded) and descriptive text (Pdf) of Fe-catalyzed CNT forest growth at ~750 °C and 200:500:10 sccm of Ar/H_2/C_2H_2 in an atmospheric tube furnace. This material is available free of charge via the Internet at http://pubs.acs.org.

References and Notes

(1) Fan, S.; Chapline, M. G.; Franklin, N. R.; Tombler, T. W.; Cassell, A. M.; Dai, H. *Science* **1999**, *283*, 512.
(2) Geohegan, D. B.; Puretzky, A. A.; Ivanov, I. N.; Jesse, S.; Eres, G.; Howe, J. Y. *Appl. Phys. Lett.* **2003**, *83*, 1851.
(3) Li, X.; Cao, A.; Jung, Y. J.; Vajtai, R.; Ajayan, P. M. *Nano Lett.* **2005**, *5*, 1997.
(4) Pinault, M.; Pichot, V.; Khodja, H.; Launois, P.; Reynaud, C.; Mayne-L'Hermite, M. *Nano Lett.* **2005**, *5*, 2394.
(5) Hart, A. J.; Slocum, A. H. *J. Phys. Chem. B* **2006**, *110*, 8250.
(6) Hata, K.; Futaba, D. N.; Mizuno, K.; Namai, T.; Yumura, M.; Iijima, S. *Science* **2004**, *306*, 1362.
(7) Murakami, Y.; Chiashi, S.; Miyauchi, Y.; Hu, M.; Ogura, M.; Okubo, T.; Maruyama, S. *Chem. Phys. Lett.* **2004**, *385*, 298.
(8) Noda, S.; Hasegawa, K.; Sugime, H.; Kakehi, K.; Zhang, Z. Y.; Maruyama, S.; Yamaguchi, Y. *Jpn. J. Appl. Phys.* **2007**, *46*, L399.

(9) Xu, Y.-Q.; Flor, E.; Kim, M. J.; Hamadani, B.; Schmidt, H.; Smalley, R. E.; Hauge, R. H. *J. Am. Chem. Soc.* **2006**, *128*, 6560.
(10) Zhang, L.; Tan, Y.; Resasco, D. E. *Chem. Phys. Lett.* **2006**, *422*, 198.
(11) Zhong, G. F.; Iwasaki, T.; Honda, K.; Furukawa, Y.; Ohdomari, I.; Kawarada, H. *Jpn. J. Appl. Phys* **2005**, *44*, 1558.
(12) Futaba, D. N.; Hata, K.; Yamada, T.; Hiraoka, T.; Hayamizu, Y.; Kakudate, Y.; Tanaike, O.; Hatori, H.; Yumura, M.; Iijima, S. *Nat. Mater.* **2006**, *5*, 987.
(13) Zhong, G. F.; Iwasaki, T.; Robertson, J.; Kawarada, H. *J. Phys. Chem. B* **2007**, *111*, 1907.
(14) Hofmann, S.; Sharma, R.; Ducati, C.; Du, G.; Mattevi, C.; Cepek, C.; Cantoro, M.; Pisana, S.; Parvez, A.; Cervantes-Sodi, F.; Ferrari, A. C.; Dunin-Borkowski, R.; Lizzit, S.; Petaccia, L.; Goldoni, A.; Robertson, J. *Nano Lett.* **2007**, *7*, 602.
(15) Cantoro, M.; Hofmann, S.; Pisana, S.; Scardaci, V.; Parvez, A.; Ducati, C.; Ferrari, A. C.; Blackburn, A. M.; Wang, K.-Y.; Robertson, J. *Nano Lett.* **2006**, *6*, 1107.
(16) Bluhm, H.; Hävecker, M.; Knop-Gericke, A.; Kiskinova, M.; Schlögl, R.; Salmeron, M. *MRS Bull.* **2007**, *32*, 1022.
(17) Seah, M. P. *Surf. Interface Anal.* **1986**, *9*, 85.
(18) Shirley, D. A. *Phys. Rev. B* **1972**, *5*, 4709.
(19) Doniach, S.; Sunjic, M. *J. Phys. C* **1970**, *3*, 285.
(20) Hofmann, S.; Cantoro, M.; Kleinsorge, B.; Casiraghi, C.; Parvez, A.; Robertson, J.; Ducati, C. *J. Appl. Phys.* **2005**, *98*, 034308.
(21) Zhang, C.; Pisana, S.; Wirth, C. T.; Parvez, A.; Ducati, C.; Hofmann, S.; Robertson, J. *Diamond Relat. Mater.* **2007**, In Press, Corrected Proof, doi:10.1016/j.diamond.2008.01.094.
(22) Arranz, A.; Perez-Dieste, V.; Palacio, C. *Surf. Sci.* **2002**, *521*, 77.
(23) Colaianni, M. L.; Chen, P. J.; Yates, J. T. *Surf. Sci.* **1990**, *238*, 13.
(24) Johnson, K. H.; Pepper, S. V. *J. Appl. Phys.* **1982**, *53*, 6634.
(25) Diebold, U.; Tao, H.-S.; Shinn, N. D.; Madey, T. E. *Phys. Rev. B* **1994**, *50*, 14474.
(26) Chase, M. W. J. *J. Phys. Chem. Ref. Data Monograph* **1998**, *9*, 1.
(27) Simmons, J. M.; Nichols, B. M.; Marcus, M. S.; Castellini, O. M.; Hamers, R. J.; Eriksson, M. A. *Small* **2006**, *2*, 902.
(28) Wang, C. M.; Baer, D. R.; Thomas, L. E.; Amonette, J. E.; Antony, J.; Qiang, Y.; Duscher, G. *J. Appl. Phys.* **2005**, *98*, 094308.
(29) Pisana, S.; Cantoro, M.; Parvez, A.; Hofmann, S.; Ferrari, A. C.; Robertson, J. *Physica E* **2007**, *37*, 1.
(30) Pretorius, R.; Harris, J. M.; Nicolet, M.-A. *Solid-State Electron.* **1978**, *21*, 667.
(31) Wen, J. M.; Evans, J. W.; Bartelt, M. C.; Burnett, J. W.; Thiel, P. A. *Phys. Rev. Lett.* **1996**, *76*, 652.
(32) Liehr, M.; Lefakis, H.; Legoues, F. K.; Rubloff, G. W. *Phys. Rev. B* **1986**, *33*, 5517.
(33) Jiran, E.; Thompson, C. V. *J. Electron. Mater.* **1990**, *19*, 1153.
(34) Gadkari, P. R.; Warren, A. P.; Todi, R. M.; Petrova, R. V.; Coffey, K. R. *J. Vac. Sci. Technol., A* **2005**, *23*, 1152.
(35) Cheung, C. L.; Kurtz, A.; Park, H.; Lieber, C. M. *J. Phys. Chem. B* **2002**, *106*, 2429.
(36) Arcos, T. d. l.; Oelhafen, P.; Thommen, V.; Mathys, D. *J. Phys. Chem. C* **2007**, *111*, 16392.
(37) Emmenegger, C.; Bonard, J. M.; Mauron, P.; Sudan, P.; Lepora, A.; Grobety, B.; Zuttel, A.; Schlapbach, L. *Carbon* **2003**, *41*, 539.
(38) Futaba, D. N.; Hata, K.; Yamada, T.; Mizuno, K.; Yumura, M.; Iijima, S. *Phys. Rev. Lett.* **2005**, *95*, 056104.
(39) Kim, D.-H.; Jang, H.-S.; Kim, C.-D.; Cho, D.-S.; Yang, H.-S.; Kang, H.-D.; Min, B.-K.; Lee, H.-R. *Nano Lett.* **2003**, *3*, 863.
(40) Maruyama, S.; Einarsson, E.; Murakami, Y.; Edamura, T. *Chem. Phys. Lett.* **2005**, *403*, 320.
(41) Dell'Acqua-Bellavitis, L. M.; Ballard, J. D.; Ajayan, P. M.; Siegel, R. W. *Nano Lett.* **2004**, *4*, 1613.
(42) Hart, A. J.; van Laake, L.; Slocum, A. H. *Small* **2007**, *3*, 772.
(43) Gunjishima, I.; Inoue, T.; Okamoto, A. *Jpn. J. Appl. Phys* **2007**, *46*, 3149.
(44) Wirth, C. T.; Hofmann, S.; Robertson, J. *Diamond Relat. Mater.* **2007**, In Press, Corrected Proof, doi:10.1016/j.diamond.2007.11.019.
(45) Zhang, L.; Li, Z.; Tan, Y.; Lolli, G.; Sakulchaicharoen, N.; Requejo, F. G.; Mun, B. S.; Resasco, D. E. *Chem. Mater.* **2006**, *18*, 5624.
(46) Smith, R. P. *Trans. Metall. Soc. AIME* **1964**, *224*, 105.
(47) Xiang, R.; Yang, Z.; Zhang, Q.; Luo, G.; Qian, W.; Wei, F.; Kadowaki, M.; Einarsson, E.; Maruyama, S. *J. Phys. Chem. C* **2008**, *112*, 4892.
(48) Meshot, E. R.; Hart, A. J. *Appl. Phys. Lett.* **2008**, *92*.
(49) Diebold, U.; Pan, J.-M.; Madey, T. E. *Surf. Sci.* **1995**, *331*−*333*, 845.
(50) Campbell, C. T. *Surf. Sci. Rep.* **1997**, *27*, 1.
(51) Robertson, J.; Sharia, O.; Demkov, A. A. *Appl. Phys. Lett.* **2007**, *91*, 132912.
(52) Michaelson, H. B. *J. Appl. Phys.* **1977**, *48*, 4729.
(53) Schlogl, R. *Angew. Chem., Int. Ed.* **2003**, *42*, 2004.
(54) Strongin, D. R.; Bare, S. R.; Somorjai, G. A. *J. Catal.* **1987**, *103*, 289.

JP802474G